

Methodologies and Implementation of Laser Powder-Bed Fusion Process Control

Ho Yeung, National Institute of Standards and Technology (NIST)

PART QUALITY in additive manufacturing (AM) is highly dependent on process control, but there is a lack of adequate AM control methods and standards. In particular, a standard programming language (such as G-code/M-code for traditional machine tools) is not well defined, and there is no uniform/transparent way of implementing laser scan strategies among the AM machine vendors. Many earlier studies of the AM process are based on the limited control parameters with access allowed by the machine vendors, such as the nominal laser scanning speed, power, and layer thickness. These studies provide invaluable information on the understanding of the AM process fundamentals but are limited by the lack of transparency of the underlying AM control implementations. Due to varying proprietary control methods, the build quality could be very different on different machines even with identical strategy/nominal control parameters. This creates great uncertainty in part qualification, and difficulty in the build process study and optimization.

Laser Control

Laser powder-bed fusion (L-PBF) (Ref 1) is one of the most-used metal AM techniques. The part is built layer by layer by scanning a high-energy laser beam to melt a cross-sectional area out of each powder layer. Figure 1

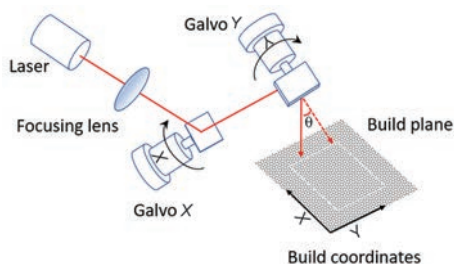


Fig. 1 Schematic showing focused laser beam guided to the build plane by a pair of mirrors driven by galvanometer (galvo) motors

shows a simplified laser system for the L-PBF process, where a focused laser beam is guided onto the flat build plane by a pair of mirrors with controllable angular position. The position of the focusing lens along the optical path is usually adjustable, allowing a variable focal distance and hence an adjustable laser spot size. The mirrors are turned by a pair of orthogonal configured galvanometer (galvo) motors, which create an X - Y coordinate on the build plane (Fig. 1). The laser power can be turned on and off by a digital input and adjusted continuously by an analog input. The laser power must be fully synchronized with the position of the laser spot to build a high-quality part. Thus, the laser control includes laser focus, laser power, laser position, and synchronization.

Laser Focus Control

While the laser beam can be positioned by rotating the mirror, this rotation also changes the focal distance from the lens to the build plane (Fig. 1). This change in focal distance can be compensated by moving the focusing lens along the laser path by a linear motor (Fig. 2a). This is known as flat-field compensation. Assuming the perpendicular distance from the rotating mirror

to the build plane is R and the scan angle is θ , moving the focusing lens to the mirror by $\Delta z = R/\cos(\theta) - R$ will keep the focal length and thus the laser spot size nominally constant. The flat-field compensation can also be achieved by an F -theta lens (Ref 2), as shown in Fig. 2(b). The focal plane of a standard focusing lens forms a curved surface, whereas the focal plane of an F -theta lens forms a flat surface. Moreover, for a standard lens, the surface travel distance x by a rotation angle θ is $F \cdot \tan(\theta)$, and for an F -theta lens is $\approx F \cdot \theta$ (Fig. 2b).

The F -theta lens simplifies the control, but the moving lens (by a linear motor) enables the active control of the laser spot size. However, if a linear motor is used for the flat-field compensation, it must continuously move according to the galvo x - and y -positions. A major challenge is that the linear motor is usually much slower than the galvo motor, due to the greater inertia. One possible solution is using both an F -theta lens for the flat-field compensation and the linear motor for the active control of the laser spot size.

The laser spot size depends on where the build plane intercepts the laser beam. Figure 3 shows a laser spot size calibration conducted on an L-PBF testbed by moving the build plane height, Z . This is equivalent to moving

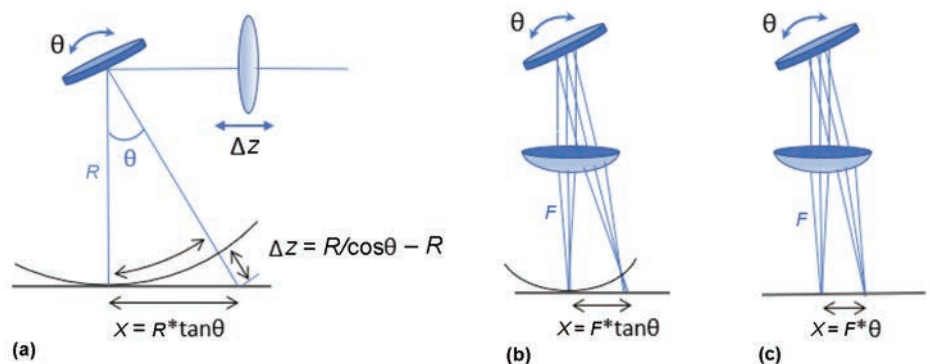


Fig. 2 Flat-field compensation. (a) Active control of focal distance. Comparison of (b) standard focusing lens (c) with F -theta lens

the focusing lens in Fig. 2(a). The larger the Z, the closer the build plane is to the focusing lens. An upward-facing pixel array is used to image the attenuated laser beam. The image is then fitted with a two-dimensional (2D) Gaussian curve to determine the D4 sigma (D4σ) diameter. The 2D Gaussian fit equation is shown in Eq 1, where the coefficient A is the amplitude; x_0, y_0 is the center; and σ_x and σ_y are the standard deviations along x- and y-axes:

$$f(x, y) = A \exp \left(- \left(\frac{(x - x_0)^2}{2\sigma_x^2} + \frac{(y - y_0)^2}{2\sigma_y^2} \right) \right) \quad (\text{Eq 1})$$

D4σ is an International Organization for Standardization standard (Ref 3) for laser diameter measurement, which is four times the standard deviation of the distribution of intensity along the axis it is measured. In Fig. 3(a), the $D4\sigma_x$ and $D4\sigma_y$ are the diameters along the major (x) and minor axes (y), respectively. $D4\sigma_{xy}$ is the average of $D4\sigma_x$ and $D4\sigma_y$. The similarity of $D4\sigma_x$ and $D4\sigma_y$ shows that there is very little elliptical distortion. Figure 3(b) shows 2D Gaussian fitting, where the mesh is the fitted function.

Laser Power Control

For a standard laser unit, the laser power is set by two voltage inputs: a digital input (DI) to turn the laser power on/off, and an analog input (AI) to set the laser power level. The output laser power can be monitored by an analog

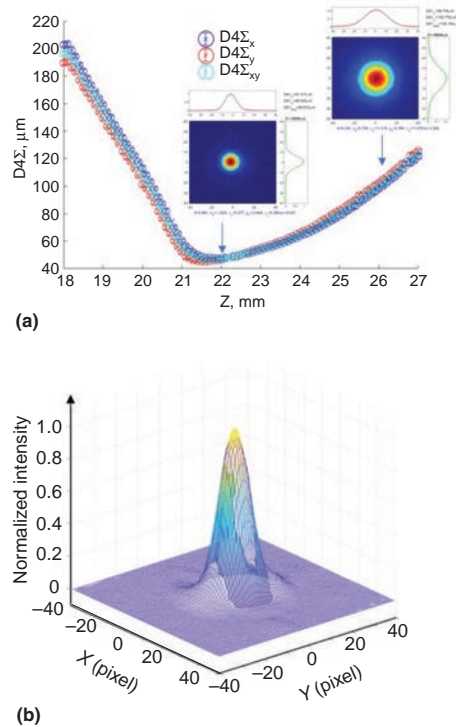
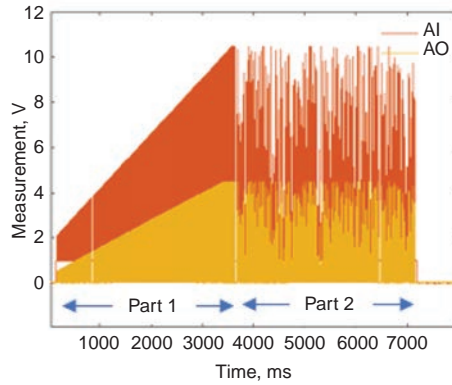
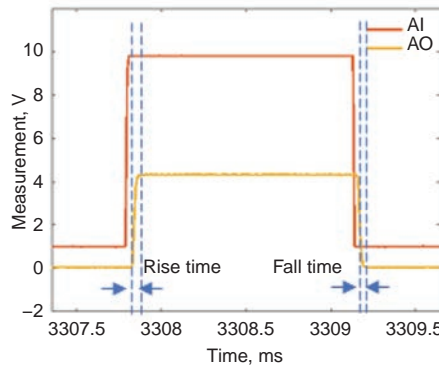


Fig. 3 Laser spot size calibration. (a) Laser beam D4σ diameter at different heights Z. Sample images are shown at Z = 22 and 26 mm (0.87 and 1.02 in.). (b) Two-dimensional Gaussian fit for a laser beam image.

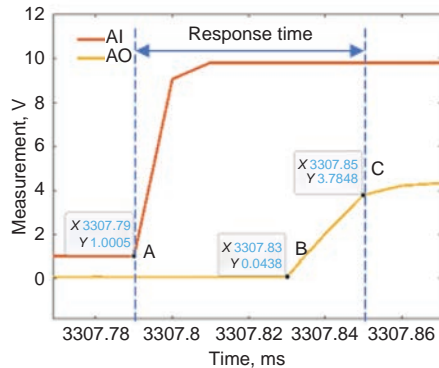
output (AO). An experiment is conducted to examine the performance of a 400 W fiber laser unit that is typical of commercial L-PBF systems based on AI and AO, while DI is left on. The AI is programmed to scan the laser power from 51 to 450 W at 1 W incremental pulse steps; for each step, the power is kept on for 1 ms (part 1). The scan is then repeated with these 400 power values in a random order (part 2). The AI and AO voltages were collected at 100 kHz and plotted in Fig. 4(a). Enlarged views around one of the pulses are



(a)



(b)



(c)

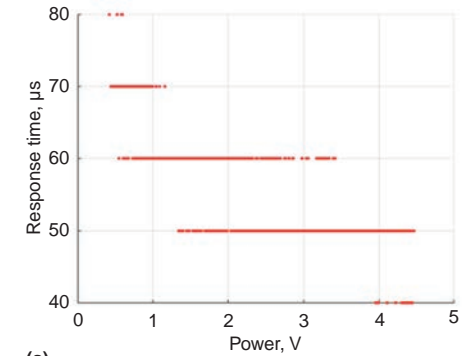
Fig. 4 Laser power control. (a) Analog input (AI) and analog output (AO) voltages plotted for full test range. (b) Expanded view showing rise and fall times. (c) Expanded view showing response time

shown in Fig. 4(b) and (c). The rise time, fall time, and response time are marked on the figures. Figure 4(c) shows there is an approximately 40 μs delay between AI and AO, and it takes another 20 μs for the laser power to rise above 80% of the nominal value. The response time here is defined as the sum of delay time and rise time. The response time is analyzed for all the 800 pulses, and the results are shown in Fig. 5(a). An external photodiode was used to verify that there is no observable delay between the AO and the actual laser beam power. Parts 1 and 2 of the data were separately analyzed and showed the same patterns.

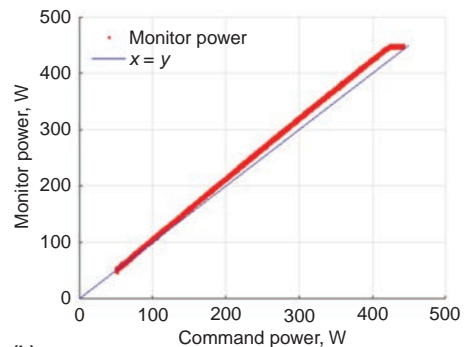
According to the manufacturing specification, an AI voltage of 1 to 10 V sets the laser power from 0 to 400 W, and an AO voltage of 0 to 4 V represents laser power of 0 to 400 W. Figure 5(b) compares the command power to the monitoring power based on these conversion scales. The relationship is quite linear but slightly off from the expected $x = y$ curve marked in the figure. A laser power meter (Ref 4) can be used for laser power measurement. A polynomial can be determined based on the measurement for more accurate AI-to-laser-power conversion. The purpose of Fig. 4 is to provide a basic understanding of a laser system performance. It provides useful information on the AM control design discussed later.

Laser Position Control

A laser beam is guided onto the build plane by a pair of mirrors turned by galvanometer



(a)



(b)

Fig. 5 (a) Laser response time for pulses in Fig. 4 at different command power levels. (b) Command power versus monitor power

motors. Figure 6 shows a conventional galvanometer. It is an instrument for measuring electrical currents by deflection of a moving coil. The electric current flowing through a coil in a magnetic field creates a torque proportional to the current. A galvo motor works using the same principle: It positions the coil based on the rotary encoder (which can be thought of as the opposite of a dial indicator in Fig. 6) feedback by applying a current/voltage across the terminals.

Therefore, a galvo motor is a limited-rotation direct current servo motor. To drive it, the digital command first must be converted into an analog signal. This is shown in Fig. 7. The digital-to-analog receiver, galvo driver, galvo motor, and mirror are usually packaged into a metal box for better mechanical

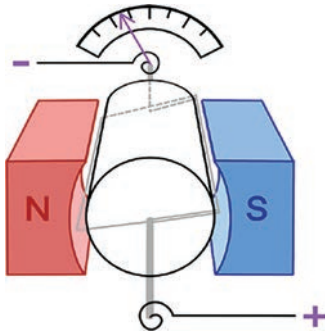


Fig. 6 Conventional galvanometer, with deflection of the coil proportional to the current flow through it

protection and electromagnetic shielding. The position command is transmitted as a digital signal to the scanner box, and analog conversion occurs locally inside the box. Digital transmission is free of transmission noise if properly implemented, which is important because galvo motors are very sensitive.

A commonly used digital transmission protocol for galvo is XY2-100 (Ref 6). It uses a DB-25 connector and can update the galvo position with a frequency up to 100 kHz. Each x-, y-, and z-position is converted into a 20-bit pack to transmit. The first 3 bits are the header, the middle 16 bits are the data, and the last bit is the parity. The transmission rate is 100 Kbps \times 20 = 2 Mbps (megabits per second). Figure 8 shows the connector wiring and timing diagram. Signals are transferred as differential pairs to minimize noise. The clock is 2 MHz, and it takes 10 μ s to transmit a 20-bit pack. The beginning of the packet is indicated by a synchronization pulse. There are also 18- and 20-bit data versions of the XY2-100 protocols that support higher resolution. The XY2-100 protocol is parallel, because each channel takes a separate pair of transmission wires. Serial protocols such as the SL2-100 (Ref 7), in which all information is transmitted through a single pair of wires, are also available.

Although the galvo rotation control is closed-loop with encoder feedback, the laser position control is open-loop because the in situ laser spot position measurement and feedback are not trivial. A galvo calibration is required to create a mapping between the galvo rotary position to the laser beam position

on the flat build plane (Fig. 2b). This can be done in two steps:

1. Create an approximated linear mapping between the galvo rotary position (θ) and the laser position (x).
2. Conduct a calibration to obtain a second-order correction polynomial for this mapping.

Figure 9 shows a typical galvo calibration method, known as the mark-and-measured method (Ref 8), in which a pattern is scanned on an anodized aluminum plate (Fig. 9a) and measured with an optical coordinate-measuring machine (Fig. 9b). The difference between the command position and measurement position can be plotted as the error map (Fig. 9c), and a correction polynomial can then be derived. An imaging-based in situ galvo calibration method can be found in Ref 9, where an optical reference is imaged by the coaxial camera to construct the actual scan path in the coordinates defined by the optical reference.

Laser Power-Position Synchronization

For an AM process, the laser power must be turned on and off at the right position and right time. This is referred to as laser power-position synchronization. Poor synchronization could result in dimensional inaccuracy and defects (Ref 10). There are two major sources of synchronization errors: poor compensation of the difference between laser power and galvo response times, and the following error in the galvo position.

A galvo scanner is a mechanical device and takes a much longer time than the laser power to respond. To synchronize the laser power to its position, a time delay (t_{delay}) must be introduced to the laser command. This delay can be estimated by a careful analysis of the control hardware or a visual inspection of a specially designed scan pattern (Ref 5). A sample scan pattern is provided in Fig. 10(a). The grid spacing is 0.2 mm (0.008 in.) and can be used

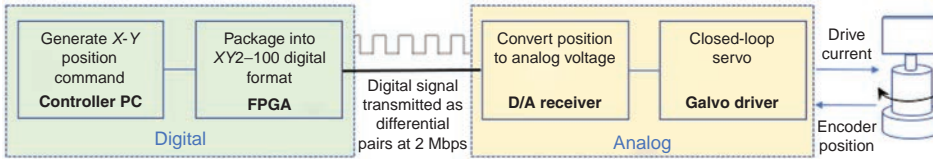


Fig. 7 Schematic showing additive manufacturing scan control. PC, personal computer; FPGA, field-programmable gate array; D/A, digital-to-analog. Source: Ref 5

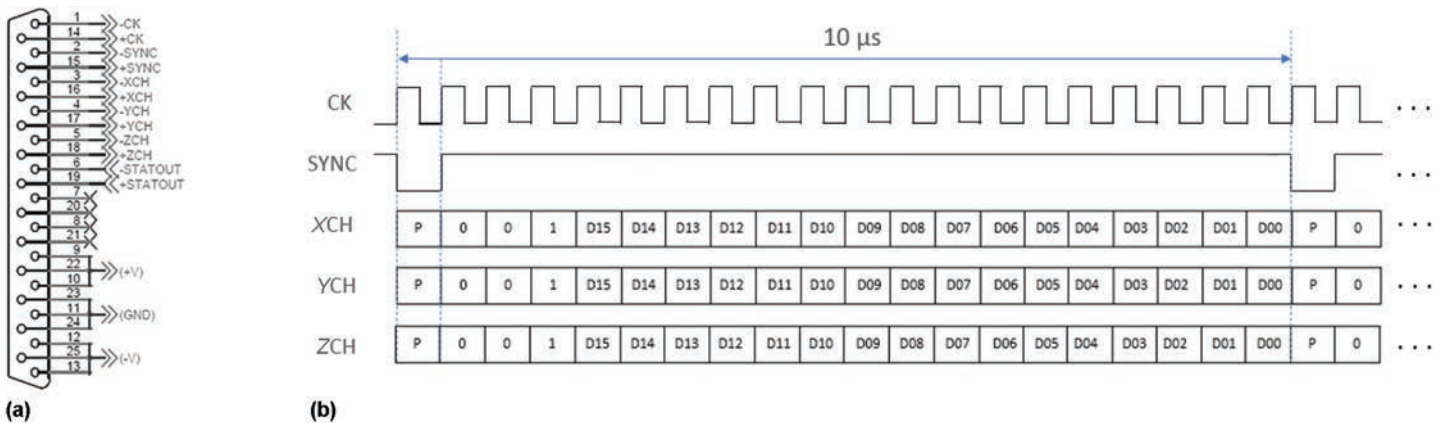


Fig. 8 XY2-100 protocol. (a) DB-25 pin layout and connector wiring. (b) Transmission timing diagram. CK, clock; SYNC, synchronization; CH, channel

as a time scale if the speed is known. The outer trapezoid provides slightly tilted boundary lines, making the small deviation more visible. Scans are conducted on black anodized aluminum sheets with different t_{delay} . Figure 10(b) and (c) compare scan patterns by $t_{\text{delay}} = 1.23$ and 1.20 ms, respectively. The lines intersect better at $t_{\text{delay}} = 1.20$ ms, as indicated by the red arrows in the blow-up regions.

Poor synchronization between laser power and position can also be caused by the following error. This occurs when the galvo cannot accelerate fast enough (Ref 10). The galvo acceleration can be tested by a swept-sine wave in Eq 2, where A is the amplitude, t is time, and $f(t)$ is the frequency:

$$X = A \cdot \sin(2\pi \cdot f(t) \cdot t) \quad (\text{Eq 2})$$

Figure 11 shows the test results, where $X_c = \sin(200 \cdot \pi \cdot t^2)$ is the commanded position, and X_m is the measured position by the galvo encoder (Fig. 7). Velocities and accelerations are the time derivatives of the positions. As

t increases, the required velocity and acceleration increase. X_m quickly lags behind X_c because the system cannot provide enough acceleration (power) to catch up. The gap between X_c and X_m is the following error. The swept-sine wave test can be used to determine the operating range of the galvo (Ref 5). Different velocity profiles can also be used to

program the scan path to lower the requirement on acceleration (Ref 11), which is discussed more in the section “AM Control Framework” in this article.

Scan Strategies

Scan strategy discussion focuses on laser scan path planning and execution. The laser control and scan strategy are closely related because the laser control enables/limits the implementation of the scan strategy. Skywrite scan strategy is used as an example to explain the consideration and limitations behind scan strategy implementation. Skywrite is a common scan strategy on commercial machines, in which the scan path is allowed to overshoot to maintain a constant speed while the laser power is on. The transient state of the scan is emphasized.

Scan Path Reconstruction

The use of the standard XY2-100 protocol provides a way to reconstruct the scan path from the digital command signal sent to the galvo scanner (Fig. 7). Figure 12 shows an example in which the digital command sent to the galvo scanner on an L-PBF additive manufacturing machine is intercepted and plotted. Figure 12(a) is the command path screen captured from the

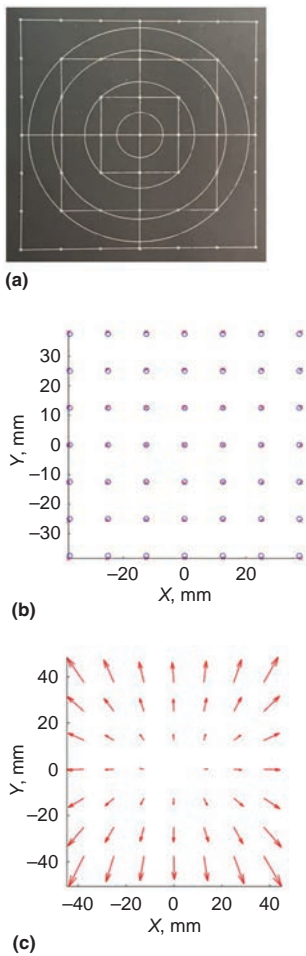


Fig. 9 Galvo calibration by mark-and-measure method. (a) Pattern marked on an aluminum plate. (b) Pattern measured by coordinate-measuring machine. (c) Error vectors (difference between commanded and measurement positions), with magnitude amplified by 10x

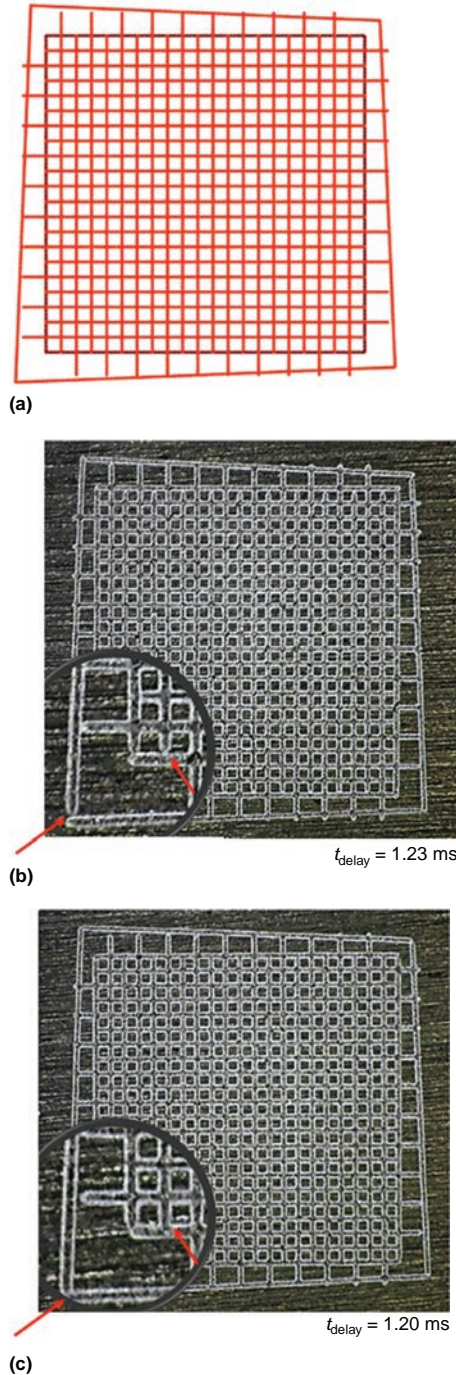


Fig. 10 Laser power-position delay calibration. (a) Scan pattern design. (b) Pattern scanned with time delay (t_{delay}) = 1.23 ms. (c) Pattern scanned with $t_{\text{delay}} = 1.20$ ms

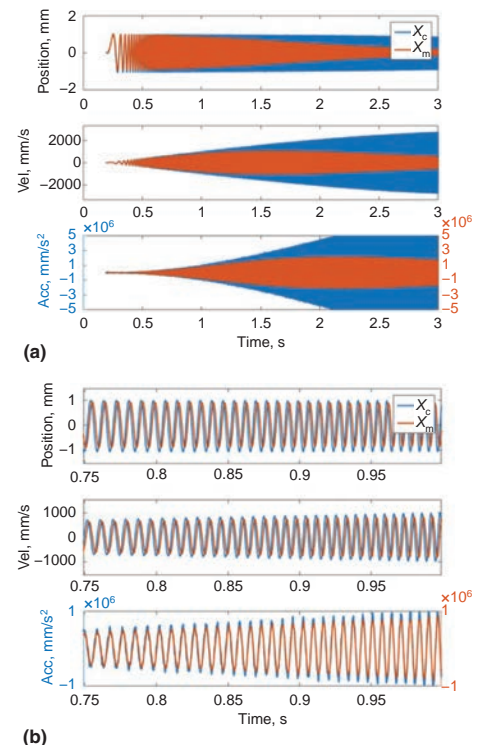


Fig. 11 Laser frequency response test. (a) Full test frequency range (0 to 300 Hz). (b) Enlarged view at approximately 75 to 100 Hz. X_c , commanded position; X_m , measured position

machine/user interface; Fig. 12(b) is the reconstructed path from the signal intercepted. Because the time interval between each point is known, the speed and acceleration can also be derived and are plotted in Fig. 12(c). The scan path reconstruction provides a tool to study the AM scan strategies on a closed-platform system in which the scan path/power information is not provided.

Skywrite Strategy

A 15 by 15 mm (0.6 by 0.6 in.) square pad was scanned on an L-PBF additive manufacturing machine with Skywrite scan strategy, with the laser speed set at 750 mm/s (30 in./s) for the infill and 400 mm/s (16 in./s) for the contour. The complete scan path is read and plotted in Fig. 13(a), and the first few hatch lines are plotted in Fig. 13(b) alongside the derived speed and acceleration. A jump in the speed/acceleration is observed at the end of each scan, making following errors unavoidable. However, this happens only when the laser power is off. This is very similar to the rapid mode in traditional machine tool control. An extension (overshoot) path is inserted at the beginning/end of each scan to allow the system to recover from the following error caused by the jump. Therefore, during the build (when the laser power is on), the scan speed remains constant. This is also referred to as constant build speed in Ref 11. Many different types of scan strategies are compared in Ref 11 and 13, and the most uniform melt pool is achieved with a constant build speed and constant laser power scan strategy. This is essentially the same as the Skywrite scan strategy.

The situation is slightly different for the contour scan in Fig. 13(c). The plots show the contour was scanned at a constant speed without overshoot (not Skywrite) and with the laser power always on. It is unlikely the galvo can follow the sharp corners with a constant speed. However, because the corner region is already melted by the infills, it will not affect the dimensional accuracy of the part.

Effect of Scan Strategy on Build Quality

The build region in Fig. 13 is divided into stripes and filled with scan lines perpendicular to the stripe boundary. One reason for striping is to keep the scan line short. Stripe strategy may be considered a subcategory of the island strategy (with long, rectangular islands). Studies show that island strategies can reduce residual stress (Ref 14–16). There are many ways to plan the scan path, but the basic rule is always to cover the building area completely. Overlaps, such as multiple contours (toward the infill regions) and extended interstripe boundaries, can also effectively

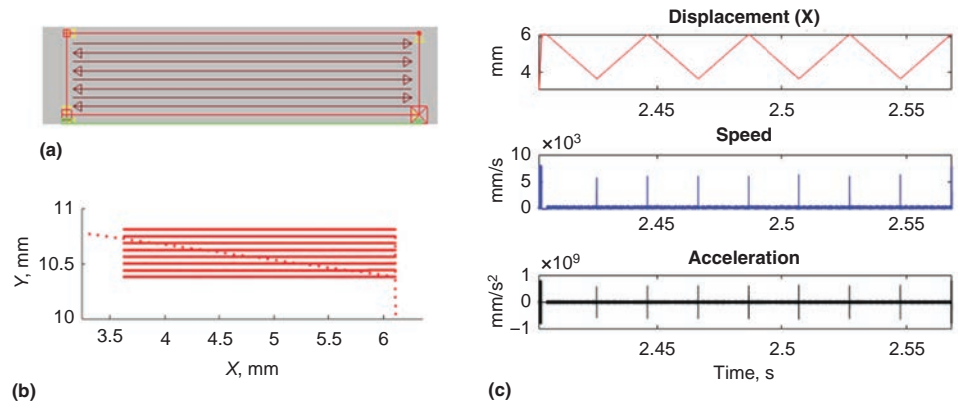


Fig. 12 Scan strategy read from a laser powder-bed fusion additive manufacturing machine for single tracks. (a) Programmed scan path. (b) Scan path constructed from intercepted digital command. (c) x -displacement, x -y speed, and x -y acceleration. Source: Ref 12

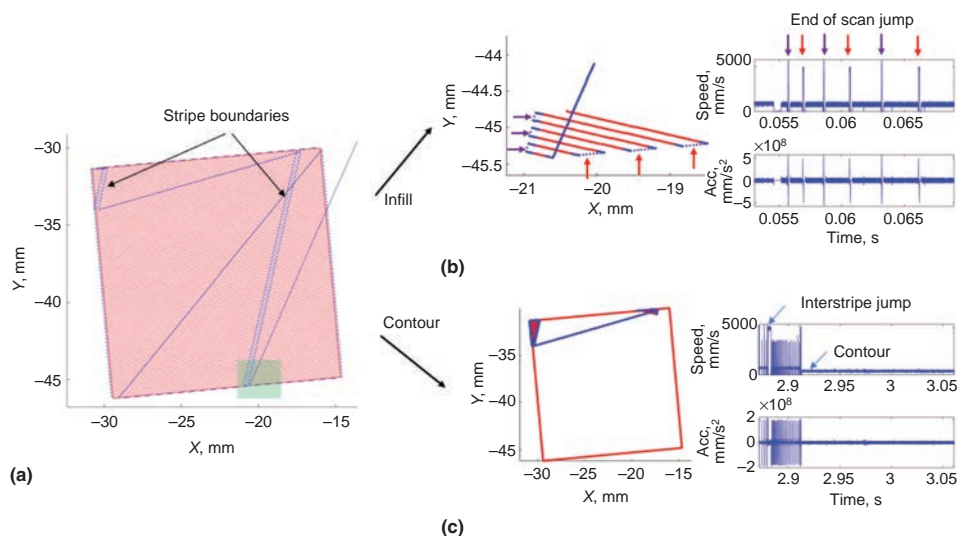


Fig. 13 Scan strategy read from a laser powder-bed fusion additive manufacturing machine for a square pad. (a) Scan path constructed from digital command intercepted. The path with laser power on is plotted in red. (b) Enlarged detail of the shaded region in (a). The end-of-scan jumps are marked by arrows on the x -y speed plot on the left. (c) Contour scan. No overshoot is observed. Source: Ref 12

correct the issues that occur at the transient state of the scan. Similarly, an interlayer rotation of hatch-line directions can help to improve the overlapping and reduce the growth of columnar grains (Ref 17). Different scan strategies can result in different residual stresses (Ref 18) and can also be used to control microstructures by changing the local thermal conditions (Ref 19).

The transient state refers to the beginning and end of a scan. The galvo needs time to accelerate and stop, and the laser needs time to reach full power (Fig. 5). Therefore, if a track is scanned, the actual laser speed/power could be very different from the steady state at the beginning and end of the scan. With typical scan parameters, a fully developed

melt pool can reach 500 to 800 μm in length, but the melt pool is much shorter at the beginning. On the other hand, switching off the laser power at the end of the scan suddenly stops the molten metal supply. Because the melt pool farther from the heating source is cooler, the surface tension pulls the molten metal back and leaves a bump at the beginning and a crater at the end. This is shown in the single-track measurement in Fig. 14. The poor laser power-speed synchronization during the transient state could also cause uneven power density and trigger a lack of fusion (Ref 10) or keyhole pores (Ref 20). Different scan strategies are developed to handle the issues caused by this transient state of the process (Ref 11).

Additive Manufacturing Control Framework

There is a lack of industry standards in AM control. Many AM machine vendors (Ref 21, 22) take proprietary approaches with their implementation. Nevertheless, the underlying technologies are believed to be the same. An open-platform AM control framework (Fig. 15) is used as a reference architecture to explain the AM control implementation. The framework consists of two major sections: software and hardware. The AM software generates time-sequenced positions (time-stepped digital commands) from a three-dimensional computer-aided design model through slicing, path/power planning, and interpolation steps. The AM hardware executes the digital commands through the synchronized actions of the laser system, powder bed, build chamber, and monitoring devices. Feedback/feedforward control loops can be implemented based on the signals from the monitoring devices. Time-stepped digital commands can also be verified/optimized by simulation before sending to build. This framework has been used to implement the Additive Manufacturing Metrology Testbed (AMMT) (Ref 12, 23) at the National Institute of Standards and Technology (NIST).

Additive Manufacturing Programming Language

The traditional computer numerical control (CNC) uses G-code (Ref 24) as the programming language. G-code describes the tool path by specifying the destination coordinate of each move. The move can be a straight line or an arc line. Therefore, G-code can be thought of as line commands. The lines are then interpreted by the machine tool controller into time-stepped digital commands to execute. The time-stepped digital commands for the tool path are simply the position coordinates updated at a regular time interval and therefore can be thought of as point commands.

Additive manufacturing galvo control technically is an example of CNC. Therefore, it seems reasonable to use G-code as the AM programming language, too. A modified G-code version for AM control can be found in Ref 18, together with its interpretation method. Another commonly used AM programming language is the Common Layer Interface (CLI) (Ref 25, 26). The CLI is designed as a universal format for the input of geometric data to model fabrication systems based on layer manufacturing technologies. It represents the scan path by contour, polyline, and hatches. Unlike G-code, CLI supports only straight lines. For both G-code and CLI, lines must be interpolated into time-stepped digital commands to execute.

Time-Stepped Digital Commands

A very important step in Fig. 15 is digital interpolation. It converts the scan lines to

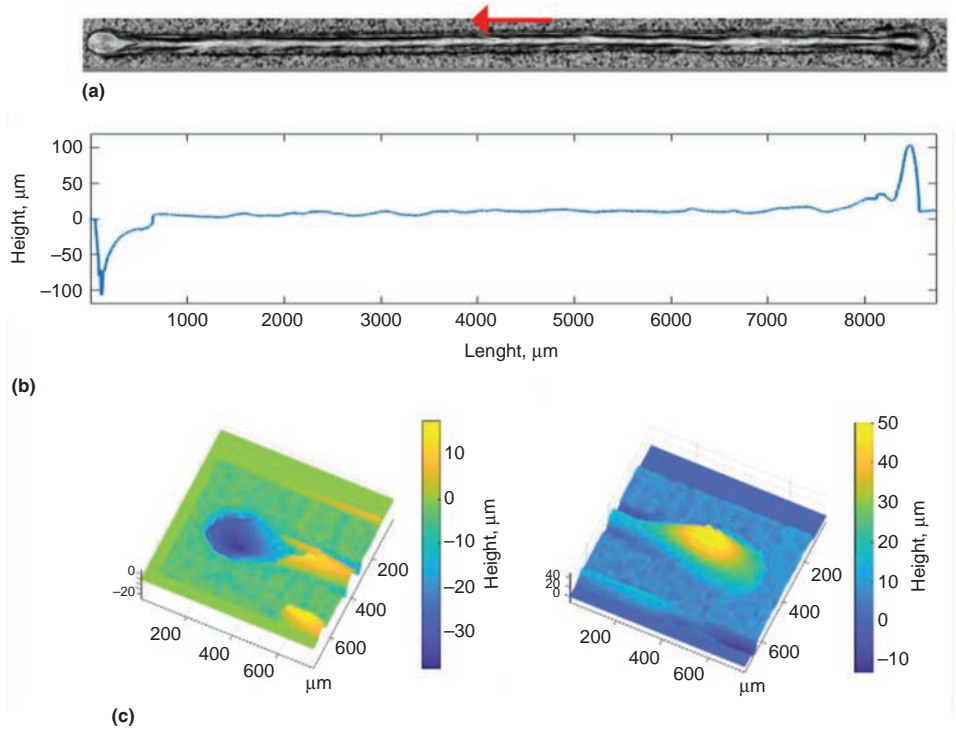


Fig. 14 Single track scanned at 500 mm/s (20 in./s) and 450 W. (a) Microscopic image of the track. Arrow indicates scan direction. (b) Cross-sectional profile along the track. (c) Surface profile at the beginning (right) and end (left) of the track

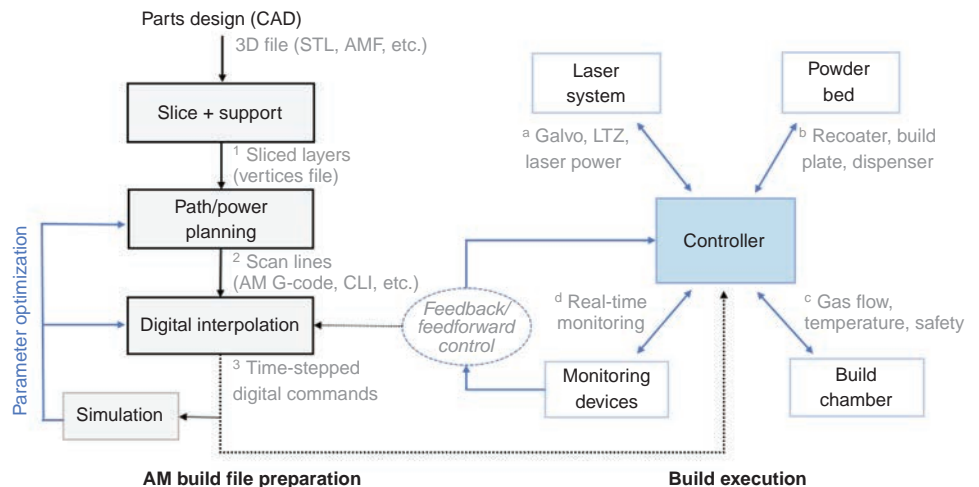


Fig. 15 Open-platform additive manufacturing (AM) process control framework that consists of four AM software modules (left side of figure) and four hardware modules (right side of figure). The interfaces (1–3) of each software module and the functionalities (a–d) of each hardware module are indicated. CAD, computer-aided design; STL, stereolithography; AMF, additive manufacturing file format; CLI, Common Layer Interface; LTZ, linear translating z-focus. Source: Ref 12

time-stepped digital commands. The XY2–100 protocol updates the x - and y -positions at 10 μ s time intervals (Fig. 8), so 10 μ s is the time step for the time-stepped digital command. Figure 16 shows an example of how the digital commands are created for a move from $Y = 0$ mm to $Y = 0.155$ mm (0.006 in.). The

displacement against time is plotted in Fig. 16 (a), and the AM G-code and time-stepped digital commands are shown in Fig. 16(e). The digital interpolation step from G-code to the time-stepped digital command can also be referred to as G-code interpretation. By differentiating the digital command with the time,

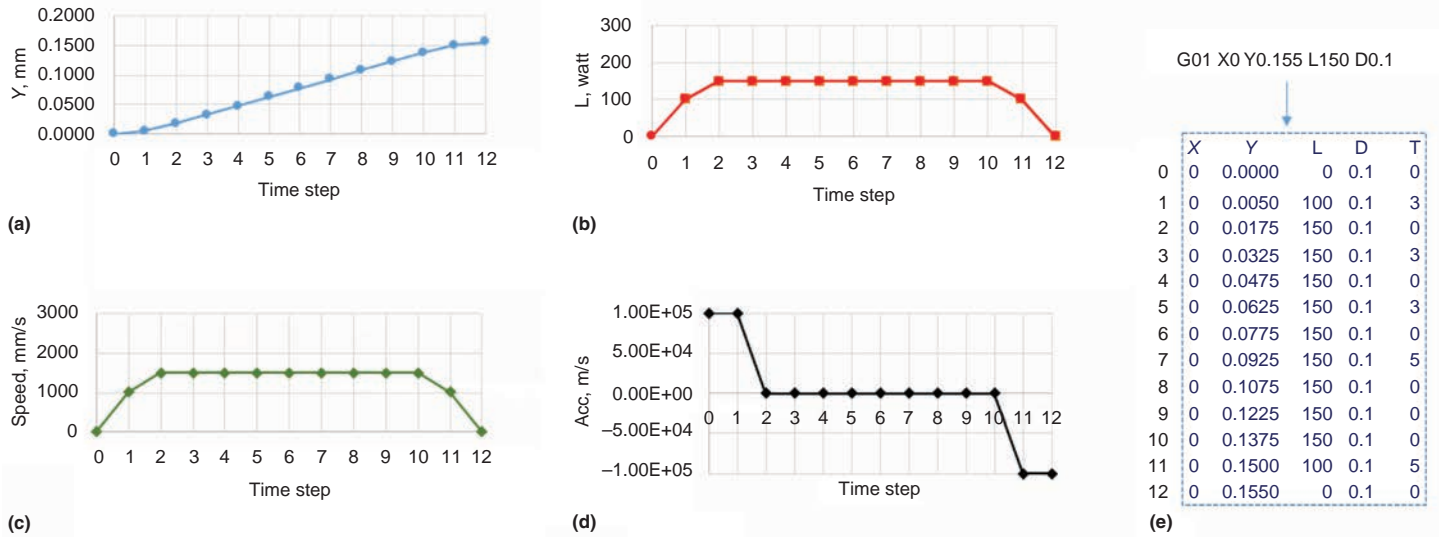


Fig. 16 Time-stepped digital command demonstration. (a) Displacement. (b) Laser power. (c) Speed. (d) Acceleration. (e) Time-stepped digital commands. L, laser power; D, laser diameter; T, trigger

the speed and acceleration profiles in Fig. 16(c) and (d) can be obtained. However, for the actual G-code interpretation process, the opposite is true. The acceleration and velocity profiles are defined first and integrated to create the time-stepped digital commands. This minimizes the following error if the acceleration is kept below the system limitation (Fig. 11).

The time-stepped digital command example in Fig. 16(e) consists not only of the laser position (X-Y) but also laser power, laser diameter, and trigger for in situ monitoring devices. Therefore, the laser power and diameter can be synchronized with each scan point. This enables the implementation of advanced scan strategies, such as commanding the laser power be proportional to laser scan speed, as shown in Fig. 16(b). The same G-code can be interpreted into different scan strategies according to different interpretation modes (Ref 11).

There is very little published information on how path interpolation is done on commercial AM machines, but from the measurements made (Fig. 12, 13), it seems step velocity is commonly used. Step velocity simplifies the path interpolation at the expense of the following error. Figure 17 is a comparison of paths with step and ramp velocity profiles. The experiments were conducted on the AMMT by NIST, and the measurements were done by reading the galvo encoder. For the path programmed by a step velocity (Fig. 17a), there is a sharp corner at the turning point (marked by a red arrow). The actual (measured) move cannot follow. For the path programmed by the ramp velocity (Fig. 17b), the corners are rounded, and the actual path follows closely after the commanded path. Similarly, a comparison of velocity shows that the ramp velocity can be

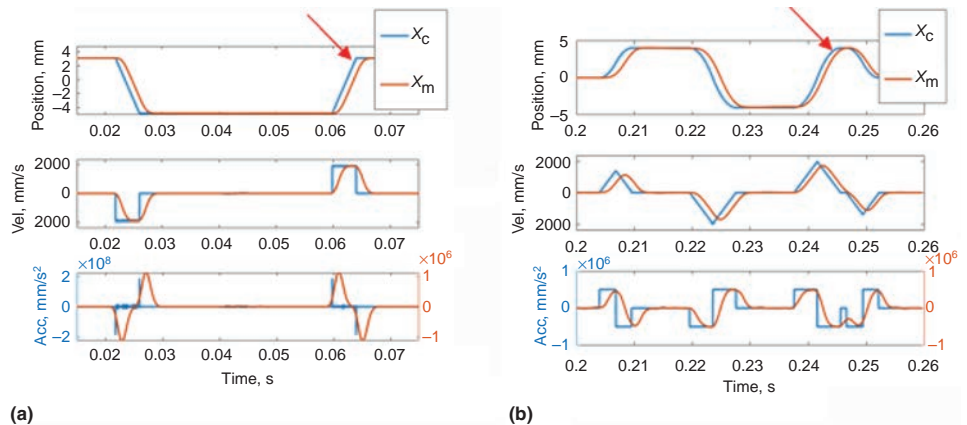


Fig. 17 Position, velocity, and acceleration graphs for (a) step velocity and (b) ramp velocity. X_c , commanded x-path; X_m , measured position

followed much more closely for the most part, except at the sharp corners.

Pointwise Control

From the time-stepped digital command perspective, the AM part can be thought of as being built point by point. For a typical scan speed of 1000 mm/s (40 in./s), each point is 10 μm apart. If laser power for each point can be individually adjusted to compensate for the variation in the local thermal condition, theoretically a uniform melt pool can be achieved. The local thermal condition will vary mainly with two factors: the local conductivity and the residual-heat accumulation. A geometric conductive factor is defined to quantify the conductivity of the as-built structure and is used to proportionally scale the laser power (Ref 27). A residual-heat factor

is also defined (Ref 19), to compensate for the residual-heat variation due to the scan sequence. These are typical examples of how pointwise laser power control can be applied to improve the build quality. Pointwise laser power control can also be based on a physical simulation model or a machine learning model (Ref 28). The open-platform AM control framework (Fig. 15) defines the time-stepped digital command as the build files to enable pointwise control.

Real-Time Feedback Control

The discussion of AM control would not be complete without real-time feedback control. Figure 18(a) shows a block diagram for a real-time feedback control loop based on a proportional-integral-derivative (PID) controller (Ref 29). A PID controller continuously calculates an error

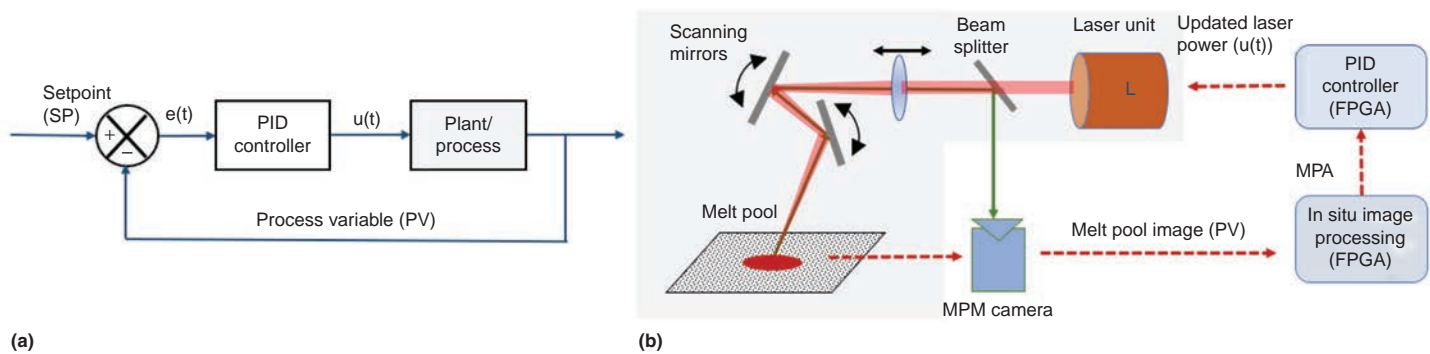


Fig. 18 Real-time feedback control design. (a) Block diagram. (b) Control loop implementation. $e(t)$, error value; PID, proportional-integral-derivative; $u(t)$, control variable; FPGA, field-programmable gate array; MPA, melt pool area; MPM, melt pool monitoring

value as the difference between the desired setpoint and a measured process variable and applies a correction on a control variable based on proportional, integral, and derivative terms (denoted “P,” “I,” and “D,” respectively).

Figure 18(b) shows the schematic for the real-time feedback control implementation on an L-PBF testbed. The control objective is to keep the melt pool area (MPA) constant by adjusting laser power, so the process variable is the MPA, and the control variable is the laser power. The melt pool images are taken by a high-speed camera and processed in situ to extract the MPA. The MPA is sent to a PID controller to update the laser power. The image processing and PID controller can be implemented with a field-programmable gate array (FPGA). A smart camera with an onboard FPGA can process melt pool images and output the MPA directly. A camera with high sensitivity can be used to reduce the exposure time. Therefore, the bottleneck for this feedback control loop is really the laser response time. Calibration in Fig. 5(a) shows that it will take approximately $60 \mu\text{s}$ for the laser to reach its updated value.

The feedback control loop response time decides its applications. If the response is fast enough, it can be applied to keep the instantaneous MPA constant. This can be used to address local/dynamic issues, such as the concentration of laser power density in transient states and a variation of residual heat due to scan sequence or overhang structure. If the loop response is slower, it can still be useful to adjust the average laser power to address the change in the global thermal condition. The process variable can also be other monitoring signals, such as a photodiode or pyrometers (Ref 30). The signal can also be processed with analytical, physical, or statistical models. One of the biggest challenges in the L-PBF process is the stochastic incidence, such as large-sized ejecta from the melt pool that may prevent the complete melting of a local area (Ref 31). In such a situation, layerwise feedback control can be used to repair (rescan) the area. Therefore, multilevel feedback control loops can be implemented.

Similarly, layerwise feedback can be used to adjust the next layer scan strategy. This can also be regarded as feedforward control.

REFERENCES

- W.E. King, A.T. Anderson, R.M. Ferencz, N.E. Hodge, C. Kamath, S.A. Khairallah, et al., Laser Powder Bed Fusion Additive Manufacturing of Metals; Physics, Computational, and Materials Challenges, *Appl. Phys. Rev.*, Vol 2, 2015, p 041304
- V.I. Yurevich, V.A. Grimm, A.A. Afonyushkin, K.V. Yudin, and S.G. Gorny, Optical Design and Performance of F-Theta Lenses for High-Power and High-Precision Applications, *Proc. SPIE Optical Systems Design* (Jena, Germany), Vol 9626, L. Mazuray, R. Wartmann, and A. P. Wood, Ed., 2015, p 96261S, <https://doi.org/10.1117/12.2190777>
- “Lasers and Laser-Related Equipment—Test Methods for Laser Beam Widths, Divergence Angles and Beam Propagation Ratios—Part 1: Stigmatic and Simple Astigmatic Beams,” ISO 11146-1:2005, International Organization for Standardization
- B. Lane, L. Jacquemetton, M. Piltch, and D. Beckett, “Thermal Calibration of Commercial Melt Pool Monitoring Sensors on a Laser Powder Bed Fusion System,” National Institute of Standards and Technology, Gaithersburg, MD, 2020, <https://doi.org/10.6028/NIST.AMS.100-35>
- H. Yeung, J. Neira, B. Lane, J. Fox, and F. Lopez, Laser Path Planning and Power Control Strategies for Powder Bed Fusion Systems, *Proc. 27th Annual International Solid Freeform Fabrication Symposium*, 2016
- J.C. Wei, G.Y. Zhang, Y. Chen, and X.T. Yan, Design of a Communication Interface between the Controller and the Galvanometer, *Appl. Mech. Mater.*, Vol 527, 2014, p 269–272, <https://doi.org/10.4028/www.scientific.net/AMM.527.269>
- S. Nieke, P. Rauscher, J. Hauptmann, T. Schwarz, and M. Mende, Solution for Real Time Sensor Guided Programmable Logic Controller of Galvanometer Scanners, *J. Laser Applic.*, Vol 33, 2021, p 042029, <https://doi.org/10.2351/7.0000477>
- W.S. Land, Effective Calibration and Implementation of Galvanometer Scanners as Applied to Direct Metal Laser Sintering, *Mater. Sci.*, 2014
- H. Yeung, B.M. Lane, M.A. Donmez, and S. Moylan, In-Situ Calibration of Laser/Galvo Scanning System Using Dimensional Reference Artefacts, *CIRP Ann.*, 2020, p S0007850620300160, <https://doi.org/10.1016/j.cirp.2020.03.016>
- F.H. Kim, H. Yeung, and E.J. Garboczi, Characterizing the Effects of Laser Control in Laser Powder Bed Fusion on Near-Surface Pore Formation via Combined Analysis of In-Situ Melt Pool Monitoring and X-Ray Computed Tomography, *Addit. Manuf.*, Vol 48, 2021, p 102372, <https://doi.org/10.1016/j.addma.2021.102372>
- H. Yeung, B.M. Lane, M.A. Donmez, J.C. Fox, and J. Neira, Implementation of Advanced Laser Control Strategies for Powder Bed Fusion Systems, *Proced. Manuf.*, Vol 26, 2018, p 871–879, <https://doi.org/10.1016/j.promfg.2018.07.112>
- H. Yeung, K. Hutchinson, and D. Lin, Design and Implementation of Laser Powder Bed Fusion Additive Manufacturing Testbed Control Software, *Proc. 32nd Annual International Solid Freeform Fabrication Symposium—An Additive Manufacturing Conference* (Austin, TX), 2021, https://tsapps.nist.gov/publication/get_pdf.cfm?pub_id=933133, accessed July 27, 2022
- B. Lane and H. Yeung, Process Monitoring Dataset from the Additive Manufacturing Metrology Testbed (AMMT): Three-Dimensional Scan Strategies, *J. Res. Natl. Inst. Stand.*, Vol 124, 2019, p 124033, <https://doi.org/10.6028/jres.124.033>
- L. Mugwagwa, D. Dimitrov, S. Matope, and I. Yadroitsev, Evaluation of the Impact of Scanning Strategies on Residual Stresses in Selective Laser Melting, *Int. J.*

- Adv. Manuf. Technol.*, Vol 102, 2019, p 2441–2450, <https://doi.org/10.1007/s00170-019-03396-9>
15. P. Bian, J. Shi, Y. Liu, and Y. Xie, Influence of Laser Power and Scanning Strategy on Residual Stress Distribution in Additively Manufactured 316L Steel, *Opt. Laser Technol.*, Vol 132, 2020, p 106477, <https://doi.org/10.1016/j.optlastec.2020.106477>
 16. R. Tangestani, T. Sabiston, A. Chakraborty, L. Yuan, N. Krutz, and É. Martin, An Efficient Track-Scale Model for Laser Powder Bed Fusion Additive Manufacturing: Part 2—Mechanical Model, *Front. Mater.*, Vol 8, 2021, p 759669, <https://doi.org/10.3389/fmats.2021.759669>
 17. M.-S. Pham, B. Dovgvy, P.A. Hooper, C.M. Gourlay, and A. Piglione, The Role of Side-Branching in Microstructure Development in Laser Powder-Bed Fusion, *Nat. Commun.*, Vol 11, 2020, p 749, <https://doi.org/10.1038/s41467-020-14453-3>
 18. M. Carraturo, B. Lane, H. Yeung, S. Kollmannsberger, A. Reali, and F. Auricchio, Numerical Evaluation of Advanced Laser Control Strategies Influence on Residual Stresses for Laser Powder Bed Fusion Systems, *Integr. Mater. Manuf. Innov.*, Vol 9, 2020, p 435–445, <https://doi.org/10.1007/s40192-020-00191-3>
 19. H. Yeung and B. Lane, A Residual Heat Compensation Based Scan Strategy for Powder Bed Fusion Additive Manufacturing, *Manuf. Lett.*, Vol 25, 2020, p 56–59, <https://doi.org/10.1016/j.mfglet.2020.07.005>
 20. R. Cunningham, C. Zhao, N. Parab, C. Kantzos, J. Pauza, K. Fezzaa, et al., Keyhole Threshold and Morphology in Laser Melting Revealed by Ultrahigh-Speed X-Ray Imaging, *Science*, Vol 363, 2019, p 849–852, <https://doi.org/10.1126/science.aav4687>
 21. V. Bhavar, P. Kattire, V. Patil, S. Khot, K. Gujar, and R. Singh, “A Review on Powder Bed Fusion Technology of Metal Additive Manufacturing,” Fourth International Conference and Exhibition on Additive Manufacturing Technologies (Bangalore, India), 2014
 22. A. Khorasani, I. Gibson, J.K. Veetil, and A.H. Ghasemi, A Review of Technological Improvements in Laser-Based Powder Bed Fusion of Metal Printers, *Int. J. Adv. Manuf. Technol.*, Vol 108, 2020, p 191–209, <https://doi.org/10.1007/s00170-020-05361-3>
 23. B. Lane et al., Design, Developments, and Results from the NIST Additive Manufacturing Metrology Testbed (AMMT), *Proc. 26th Annual International Solid Freeform Fabrication Symposium*, 2016
 24. “Interchangeable Variable Block Data Format for Positioning, Contouring, and Contouring/Positioning Numerically Controlled Machines,” EIA RS-274-D, Electronic Industries Association, 1979
 25. Common Layer Interface (CLI): Version 2.0, Commission of the European Communities, 1994
 26. Common Layer Interface (CLI), https://www.hmilch.net/downloads/cli_format.html
 27. H. Yeung, B. Lane, and J. Fox, Part Geometry and Conduction-Based Laser Power Control for Powder Bed Fusion Additive Manufacturing, *Addit. Manuf.*, Vol 30, 2019, p 100844, <https://doi.org/10.1016/j.addma.2019.100844>
 28. H. Yeung, Z. Yang, and L. Yan, A Melt-pool Prediction Based Scan Strategy for Powder Bed Fusion Additive Manufacturing, *Addit. Manuf.*, Vol 35, 2020, p 101383, <https://doi.org/10.1016/j.addma.2020.101383>
 29. K.J. Åström and T. Hägglund, *PID Controllers*, 2nd ed., International Society for Measurement and Control, Research Triangle Park, NC, 1995
 30. B. Lane, E. Whinton, and S. Moylan, Multiple Sensor Detection of Process Phenomena in Laser Powder Bed Fusion, *Proc. SPIE Commercial and Scientific Sensing and Imaging* (Baltimore, MD), J.N. Zalameda and P. Bison, Ed., 2016, p 986104, <https://doi.org/10.1117/12.2224390>
 31. A.R. Nassar, M.A. Gundermann, E.W. Reutzel, P. Guerrier, M.H. Krane, and M.J. Weldon, Formation Processes for Large Ejecta and Interactions with Melt Pool Formation in Powder Bed Fusion Additive Manufacturing, *Sci. Rep.*, Vol 9, 2019, p 5038, <https://doi.org/10.1038/s41598-019-41415-7>